Measurements of poloidal rotation velocity using charge exchange spectroscopy in a large helical device

K. Ida,[a] S. Kado, and Y. Liang
National Institute for Fusion Science, Oroshi-cho, Toki-shi, Gifu 509-5292, Japan

(Received 26 October 1999; accepted for publication 16 February 2000)

Absolute measurements of poloidal rotation velocity with the accuracy up to 1 km/s (2 pm in wavelength) were done using charge exchange spectroscopy in a large helical device. Radial profiles of the absolute Doppler shift of charge exchange emission with a beam are obtained from spectra measured with four sets of optical fiber arrays that view downward and upward at the poloidal cross section with and without neutral beam injection. By arranging the optical fiber from four arrays close to each other at the entrance slit, the apparent Doppler shift due to aberrations of the spectrometer and due to interference of the cold component (the charge exchange between He-like oxygen and thermal neutrals 8 pm from the charge exchange emission with a beam) can be eliminated from the measurements. The measured poloidal rotation velocity is 1–3 km/s in the electron diamagnetic direction at half of the plasma minor radius. © *2000 American Institute of Physics.* [S0034-6748(00)04006-5]

I. INTRODUCTION

The radial electric field has been recognized as being important in a heliotron/torsatron because neoclassical transport is very sensitive to the radial electric field. Charge exchange spectroscopy (CXS) has been developed as a tool to measure ion temperature profiles[1–9] and plasma rotation and also the radial electric field using radial force balance.[10–12] In a heliotron/torsatron, there is no large toroidal rotation because of parallel viscosity in the toroidal direction.[13] Therefore, the radial electric field is mainly determined by the poloidal rotation.[14–16] The poloidal rotation (v_θ) as well as ion temperature (T_i) of fully ionized carbon are measured with CXS using heating neutral beam injection (NBI) in a large helical device (LHD). Because of the negative ion source of the NBI, the operating energy range of heating neutral beam is relatively high ($E_{\mathrm{NBI}}=100-180$ keV/amu). Therefore, the charge exchange cross section between the fully ionized impurity and hydrogen atom in a LHD is much smaller ($E_{\mathrm{NBI}}=40-60$ keV/amu) than that in charge exchange spectroscopy using a heating neutral beam with medium energy ($E_{\mathrm{NBI}}=40-60$ keV/amu) in most large tokamaks. The small charge exchange cross section due to the high energy beam in a LHD makes the CXS measurements difficult, because (1) the number of photons in charge exchange emission is small and (2) the ratio of the charge exchange emission signal to the background emission (the S/B ratio) is small.

II. CHARGE EXCHANGE SPECTROSCOPY SETUP

In order to solve the problem of a small number of photons, a large throughput Czerny–Turner spectrometer (focal length of 0.5 m, F number of 4, grating size of 110 mm $\times$110 mm) and a cooled charge coupled device (CCD)[7] with long integration time have been developed for CXS in a LHD. The background emission is mainly due to the charge exchange reaction between the fully ionized impurity and the thermal neutrals near the plasma edge and is called the cold component. In order to precisely measure the cold component at the poloidal cross section without NBI, simultaneous measurements of the cold component of each chord are required in a LHD.

Four sets of optical fiber arrays (11 fibers each) with a 0.2 mm core diameter and a 0.25 mm clad diameter were installed into the port where one can view the NBI path (CXS channels), while the other two sets of optical fiber arrays were installed into the port where one cannot view the NBI path [background (BKG) channels] as seen in Fig. 1. The charge exchange emissions due to the neutral beam (hot component) are extracted by subtracting the cold components[6] measured at BKG channels from the overall signal measured at CXS channels. Since the emission measured at the CXS channels includes both hot component emitted from the intersection between the line of sight and the neutral beam at midplane and cold component emitted from the plasma edge, the ion temperature estimated from the overall signal measured at CXS channels is underestimated. The influence of the cold component on poloidal rotation measurements is more complicated and the poloidal rotation simply derived from a overall signal can be either underestimated or overestimated depending on the direction of the poloidal rotation velocity of the cold component. The absolute values of the poloidal rotation velocity are derived from the differences in the Doppler shift measured from the two arrays, one viewing upward and the other viewing downward. These optical fibers are led to the entrance slit of the spectrometer through an optical fiber junction box, which enables us to change the fiber arrangement easily. The optical fibers from four different ports are arranged as shown in Fig. 1. The charge exchange channels and background chan-

[a]Electronic mail: ida@nifs.ac.jp

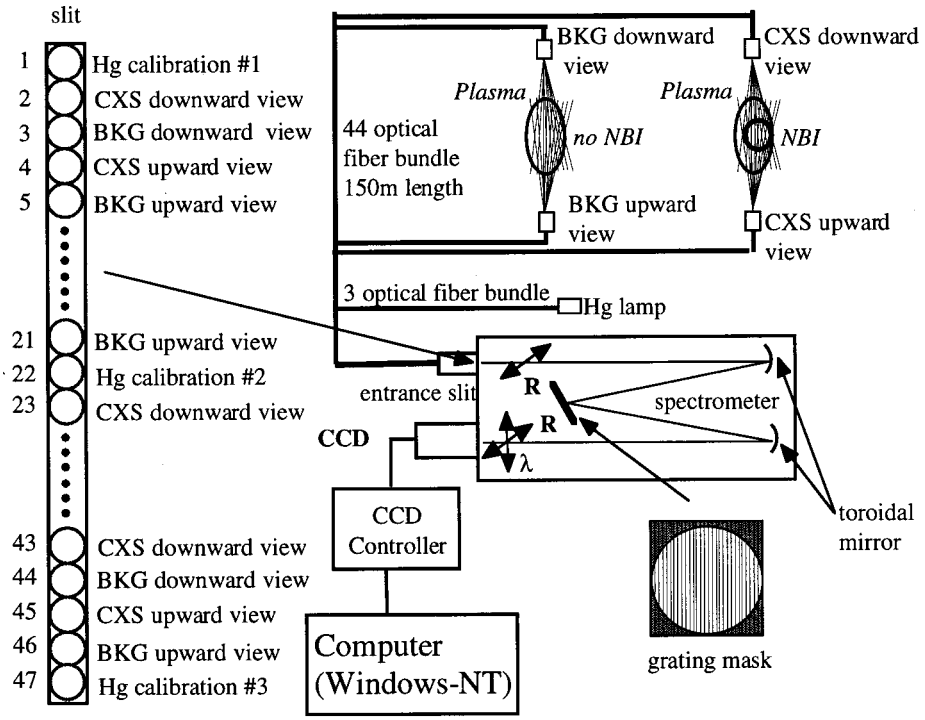

FIG. 1. Schematics of charge exchange spectroscopy for the measurements of poloidal rotation velocity and the curve of the wavelength shift due to aberrations of the spectrometer at $\lambda = 546.07$ nm.

nels that view identical radii to those of the charge exchange channel are arranged nearby to minimize offset of the wavelength due to aberrations of the spectrometer in subtracting the cold component from charge exchange emission. The offset of the wavelength due to the aberrations[5,6] caused by the mirrors is expressed as $\delta\lambda \propto \lambda(z/f)^2$, where λ is the measured wavelength, z is the distance from the optical axis, and f is the focal length. The offset is largest at the end of fiber array and it is 0.003 nm/strip (1/50–1/100 of the Doppler width); it has a negligible effect on the ion temperature measurements. However, in the measurements of poloidal rotation velocity, even the small offset of the wavelength causes an apparent poloidal rotation velocity (2 km/s for 0.003 nm offset). In order to measure the offset curve, three channels of the optical fiber (both ends and the middle one of the fiber array) are devoted to wavelength calibration using a mercury lamp. In principle, an accurate poloidal rotation velocity can be obtained by taking the differences of the Doppler shift between the measurements and offset curve calibrated with a mercury lamp. However, the absolute wavelength of the charge exchange line is determined within an accuracy of 0.01 nm. Therefore the poloidal rotation velocity is derived from the differences between the Doppler shifts measured with two arrays viewing upward and downward. In a LHD, the observation radii of the array viewing downward are arranged to be in between those of the array viewing upward. Then the wavelength offset due to the aberrations can be almost canceled simply by taking the difference of the Doppler shift from the average of Doppler shift nearby. For example, poloidal rotation velocity, *vp,* for channel 4 is derived from the velocity of the Doppler shift, vs, of channels 4, 2 and 6, as $vp(4) = [vs(4) - (vs(2) + vs(6)]/2)/2$. The linear interpolation is good approximation, because the offset that was calculated from the average of ± 2 channel is almost identical to that calculated from the aberration curve. The individual offset beside the aberration of the spectrometer is 0.14 pixel [root mean square (rms)] [see Fig. 3(a)], which gives an error in poloidal rotation velocity of 1.5 km/s. This linear interpolation gives the smoothing in three spatial channels and the poloidal rotation velocity might be underestimated due to the smoothing effect, when there is a sharp gradient of poloidal rotation velocity in the plasma in three channels.

III. CROSSTALK AND ABERRATIONS OF THE SPECTROGRAPH

Since one optical fiber gives one spatial channel, the number of spatial channels increases as the diameter of the optical fiber is reduced. However an optical fiber with a smaller diameter causes larger crosstalk between the channels. Therefore the crosstalk should be investigated before determining the diameter of the optical fiber array at the entrance slit. In order to study the crosstalk, the vertical (parallel to the slit) image is measured at 546.07 nm using a mercury lamp for the 0.132ϕ optical fibers (0.132 mm clad diameter and 0.106 mm core diameter) and 0.25ϕ optical fibers (0.25 mm clad diameter and 0.2 mm core diameter) installed along every other entrance slit. The image of the optical fiber with a 0.106 mm core diameter corresponds to five pixels and no flat top of the intensity is observed, because the size of the optical fiber is comparable to the vertical resolution of the spectrometer. On the other hand, the image of the optical fiber with a 0.2 mm core diameter correspond to nine pixels and there is a clear flat top of the observed intensity. There are signals on the pixels where no optical fiber is connected (no light from the mercury lamp), which causes crosstalk between the channels. Here crosstalk

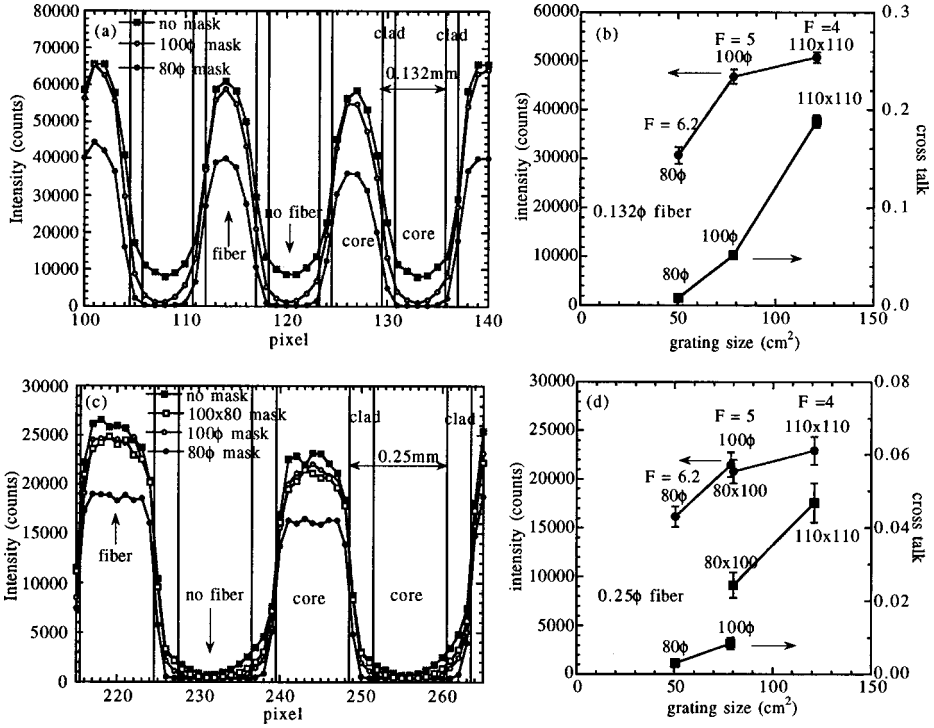

FIG. 2. Vertical profiles of the fiber image of the optical fiber with diameters of (a) 0.125 and (b) 0.25 mm at $\lambda = 546.07$ nm and crosstalk as a function of grating size (the F number of the spectrometer) of the optical fiber with diameters of (c) 0.125 and (d) 0.25 mm.

is defined as the averaged intensity of the five (nine) pixels corresponding to the core where no fiber is connected divided by that corresponding to the core where the fiber is connected. In general, the sharpness of the vertical image can be improved as the F number is increased by putting a mask on the grating. Here the F number of the spectrometer is defined by $(4S/\pi)^{1/2}/f$, where S is the area of grating and f is the focal length of the spectrometer. Figure 2 shows the how the sharpness of the vertical image is improved by putting the three types of masks with the aperture of the 100ϕ circle, the 80ϕ circle and the 80 mm (horizonal)$\times$100 mm (vertical) square on the grating.

When there is no mask on the grating, the crosstalk is relatively large and it is 20% for the 0.132ϕ optical fiber and 5% for the 0.25ϕ optical fiber. The throughput of the light of the spectrometer increases as the size of the grating increases. However, the throughput tends to saturate above $F = 5$. This is because light far from the optical axis does not contribute to an increase in the intensity of the image but causes crosstalk. The crosstalk is significantly reduced to 5% (100ϕ mask) and 0.8% (80ϕ mask) for the 0.132ϕ optical fiber and 2.4% (80 mm$\times$100 mm), 0.8% (100ϕ mask), and 0.3% (80ϕ mask) for the 0.25ϕ optical fiber by masking. Figure 2(d) shows the advantage of the mask with a circular aperture over the mask with a square aperture. Although the throughput of the light with a 100ϕ mask is comparable to that with a 80 mm$\times$100 mm mask, the crosstalk for the 100ϕ mask is much smaller than that for the 80 mm$\times$100 mm mask by a factor of 3. This is because the light closer to the optical axis is more beneficial. In charge exchange spectroscopy in a LHD, the mask with a 100ϕ circular aperture and 0.25 mm optical fibers is installed in the spectrometer to reduce the crosstalk to below 1%. The spatial resolution of the spectrometer with a mask of 100ϕ diameter is 0.13 mm for the MFT=5% and 0.24 mm for the MFT=1%. Crosstalk of 1% is considered to be low enough, because the ratio of the hot component to the cold component is typically 20%–100%, as discussed later.

The CCD detector is 8.45 mm (horizontal direction) $\times$12.67 mm (vertical direction) with 384$\times$576 pixels (the size of each pixel is 22 μm$\times$22 μm), which gives the simultaneous measurement of spectra with a wavelength range of 7.1 nm and slit height of 12.67 mm. In order to make a one to one correspondence between the strip of the CCD and the spectra from each optical fiber with a 0.2 mm core and a 0.25 mm clad, the CCD data are read out with nine pixel binning and three pixel skipping as seen in Fig. 2(c). This binning pattern gives 48 strips from 576 pixels: 22 strips are used for charge exchange emission, 22 strips for background emission and 3 strips for Hg lines to check aberrations (1 strip is not used). The readout time of the CCD detector depends on the number of binnings, and it is 65 ms for 48 strips. During the readout the mechanical shutter is closed to avoid smearing. Since shutter opening/closing takes 5–10 ms, there is roughly 80 ms dead time in this system. Therefore the integration time is normally set to 100 ms (for a frame rate of 10 Hz) or to 900 ms (for a frame rate of 1 Hz) depending on the intensity of the charge exchange emission.

As discussed before, the offset of the wavelength due to aberrations caused by the mirrors is expressed with a second order polynomial of strip number and it is measured with Hg lines ($\lambda = 546.07$ nm). As shown in Fig. 3(a), the offset of the wavelength due to aberrations is well fitted by the a second order polynomial. Then only the three strips are devoted to the Hg lines during experiments, because three points are enough to give a second order polynomial fitting curve.

The uniformity of the cold edge component can be checked with the discharges where there is no neutral beam. (The long pulse discharges sustained by ion cyclotron range of frequency (ICRF) heating are ideal for this check and can

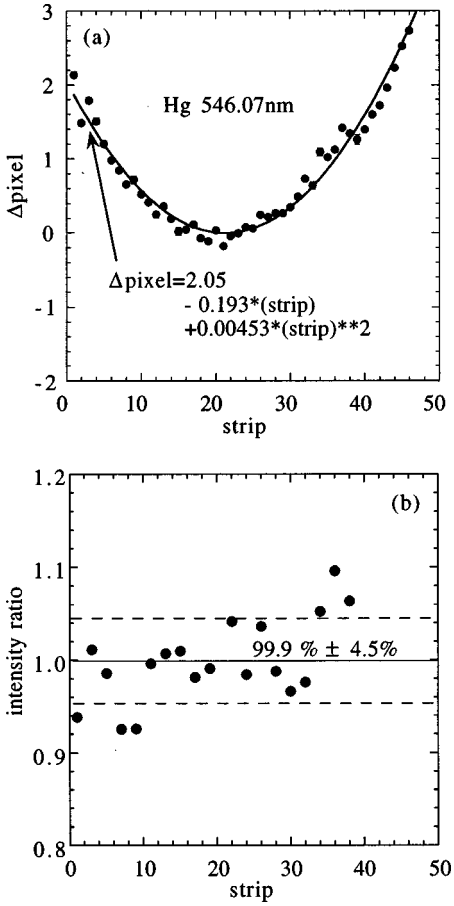

FIG. 3. (a) The curve of the wavelength shift due to aberrations of the spectrometer at $\lambda = 546.07$ nm and (b) the radial profiles of the intensity ratio (the ratio of the emission from the CXS channels to that of emission from the BKG channels) for the discharge without a neutral beam.

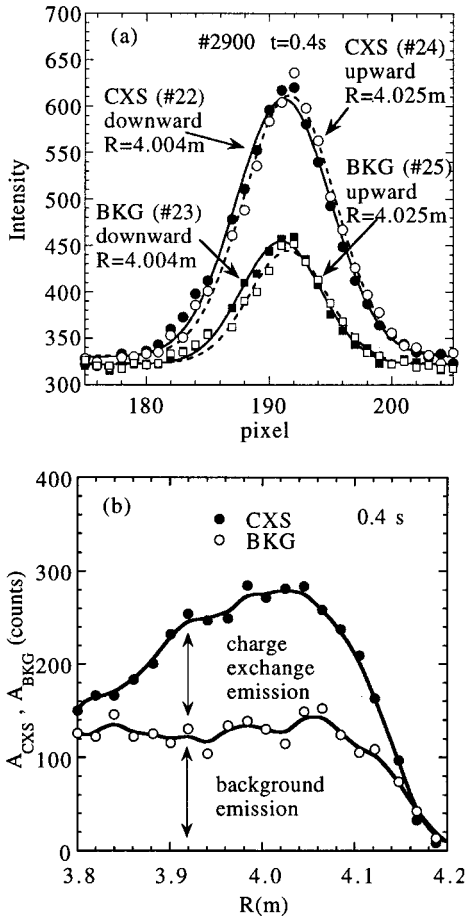

FIG. 4. (a) Spectra of charge exchange emission and background emission at $R = 4.004$ m (downward view: channels 22 and 23) and $R = 4.025$ m (upward view: channels 24 and 25) and (b) radial profiles of the peak intensity of a charge exchange array and a background array.

be used for calibration if necessary.) The radial profiles of the intensity ratio (the ratio of the emission from the CXS channels to that of emission from BKG channels) are plotted in Fig. 3(b). The uniformity of the cold edge component is relatively good. When there is no beam, the ratio of emission for charge exchange channels to that of background channels is close to unity and it is 99.9%±4.5% (rms). A local nonuniformity appears when a limiter is inserted to the same port to that of charge exchange channels or background channels because of a local increase of neutral density. Then the measurements of ion temperature and poloidal rotation velocity are restricted to discharges with a diverter configuration. The gas puff valves are installed in the port away from the CXS or BKG ports to avoid a local increase of neutral density in the LHD. In general, the transmission of windows decreases in time. To minimize contamination of the glass window due to electron cyclotron resonance (ECR) or glow discharges, the mechanical shutters are arranged in front of the window.

IV. SPECTRA OF THE C VI CHARGE EXCHANGE LINE AND OVERLAPPED O VI LINE

The charge exchange line of fully ionized carbon C VI (529.05 nm, $\Delta n = 8-7$) is typically used for the measurements. Figure 4 shows the spectra of C VI of the CXS channel and the background channel of the downward viewing array ($R = 4.004$ m) and the upward viewing array ($R = 4.025$ m). The C VI spectra of the downward viewing array show a blueshift, while the C VI spectra of the upward viewing array show a redshift, which indicates that the plasma rotates in the upward direction at $R > R_{\text{axis}}$. The Doppler width of the BKG channel is smaller than that of the CXS channel because the background emission due to the charge exchange between fully ionized carbon and thermal neutral comes from the plasma edge where the ion temperature is low. The cold component of fully ionized carbon is comparable to the charge exchange emission (CXS intensity to BKG intensity) at $R = 4.0$ m, where the center of the neutral beam crosses. The differences in the Doppler shift between upward view and downward view arrays which are observed both in the CXS channels and BKG channels are mainly due to plasma poloidal rotation. The differences in the Doppler shift of BKG channels indicate there is non-negligible poloidal rotation at the plasma edge. The charge exchange emission is even smaller than the background emission ($A_{\text{CXS}}/A_{\text{BKG}} < 2$) off the center of NBI. Subtraction of the cold component from the charge exchange emission is necessary for C VI in a LHD. The ion temperature derived from charge exchange emission without subtraction is much lower

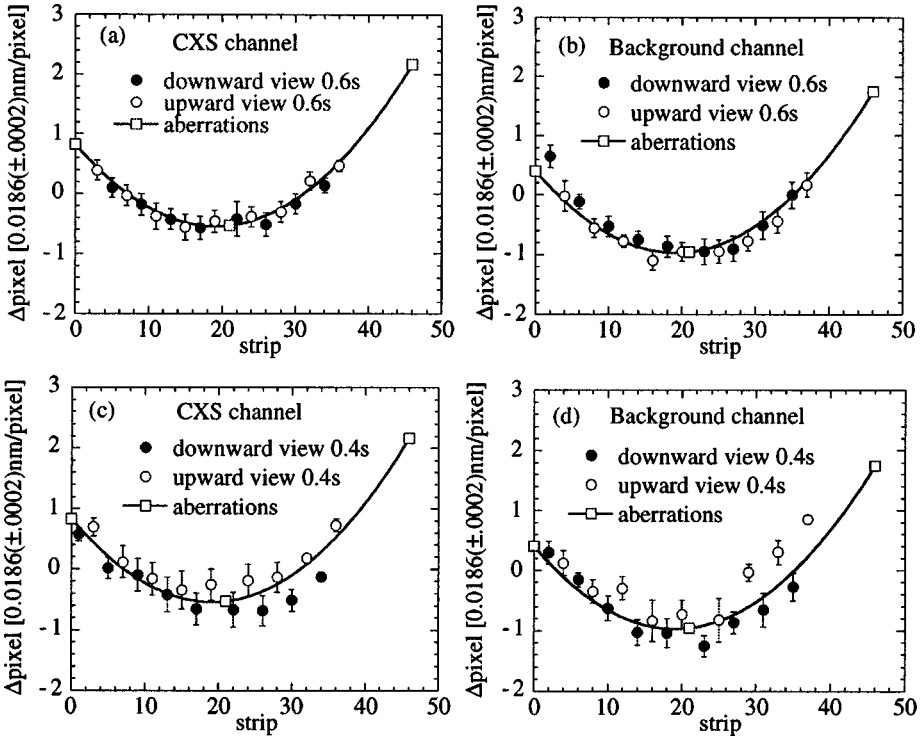

FIG. 5. Radial profiles of the wavelength shift of CXS channels and the background channel at $t=0.4$ and 0.6 s. Closed and open circles are wavelength shifts of the C VI line viewing downward and viewing upward, respectively, while the open squares and solid lines represent mercury lamp data (530.4086 nm: second order of the 265.2043 nm Hg line) and the curve of the wavelength shift due to aberrations of the spectrometer.

than that with subtraction. Measurements of radial profiles of poloidal rotation velocity are more difficult than those of ion temperature because the Doppler shift due to poloidal rotation is less than 1/20 of the Doppler width in a LHD. The Doppler shift is even smaller than the wavelength shift due to aberrations, as discussed before.

Figure 5 shows the wavelength shift of charge exchange channels and the background channel at $t=0.6$ s when there are only small plasma poloidal rotations and $t=0.4$ s when significant poloidal rotation is observed. The solid lines show fitting of the mercury lamp data (530.4086 nm: second order of the 265.2043 nm Hg line) with a second order polynomial. When there is no poloidal rotation velocity at $t=0.6$ s, the wavelength shift of C VI lines is on the aberrations curve of the spectrometer calibrated by the mercury lamp, seen in Figs. 5(a) and 5(b). On the other hand, at $t=0.4$ s, poloidal rotation is observed in the differences between the wavelength shift from the array viewing upward and downward (open and closed circles) seen in Figs. 5(c) and 5(d). The apparent shift of the wavelength due to aberrations is larger than that due to poloidal rotation of the plasma. These data show that a central wavelength of charge exchange emission is different from that of background emission by 8 pm. Here the absolute wavelength is determined by the reference wavelength Hg line from the mercury lamp (530.4086 nm: second order of the 265.2043 nm Hg line), which can be measured simultaneously with the carbon charge exchange line (529.05 nm) during the experiment.

In order to study the mechanism of the wavelength shift, the fine structure of charge exchange emission[4] for the possible charge transfer process is investigated using the atomic data and analysis structure (ADAS). The hot component of charge exchange emission is due to the charge exchange between the fully ionized carbon and the neutral hydrogen atom of the high energy neutral beam (beam C VI line) as

$$H^0_{\text{beam}}\ (n=1)+C^{6+}\rightarrow H^+ + C^{5+}\ (n=8).$$

On the other hand, the cold component radiated from the plasma edge is considered to be due to the charge exchange

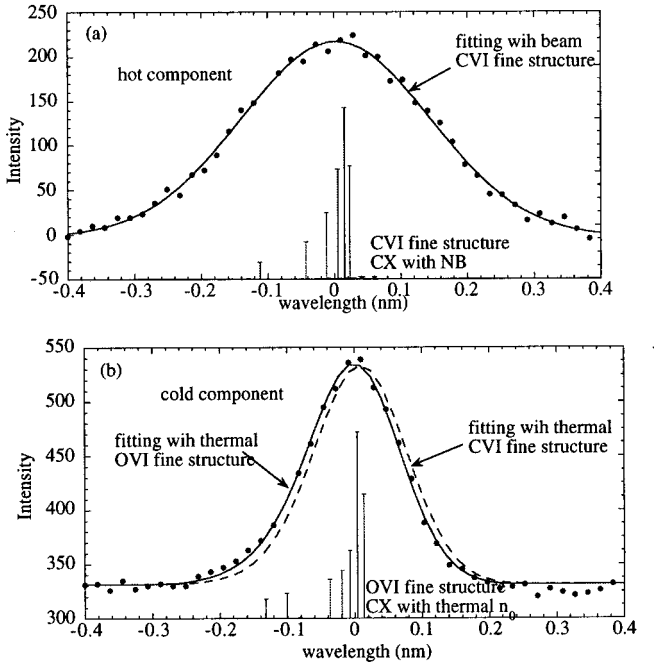

FIG. 6. Spectra of the hot component and background emission at $R=4.004$ m at $t=0.6$ s. The solid and dashed lines are multi-Gaussian fittings of the fine structure of C VI and O VI lines, where $d\lambda=\lambda-529.055$ nm.

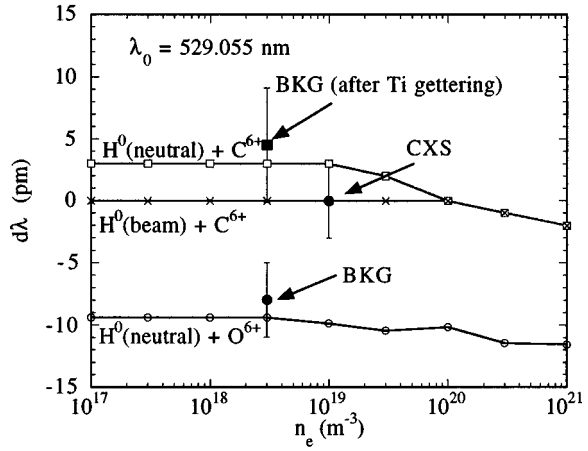

FIG. 7. Mean wavelength of charge exchange emission for H^0 ($n=1$) (80 keV beam) + C^{6+}, H^0 ($n=2$) (0.2 keV thermal neutral) + C^{6+}, and H^0 ($n=2$) (0.2 keV thermal neutral) + O^{6+} as a function of electron density with the experimental data from CXS and BKG channels shown in Fig. 4. The mean wavelength of charge exchange emission of BKG channels after Ti gettering.

between fully ionized carbon (thermal C VI line) or helium-like oxygen (thermal O VI line) and thermal neutral hydrogen atom as

$$H^0_{\text{thermal}}\ (n=2)+\text{C}^{6+}\rightarrow\text{H}^{+}+\text{C}^{5+}\ (n=8),$$

$$H^0_{\text{thermal}}\ (n=2)+\text{O}^{6+}\rightarrow\text{H}^{+}+\text{O}^{5+}\ (n=8).$$

Figure 6 shows the spectra of the hot component and the cold component with the fine structure of these processes. The hot component is obtained by subtracting the emission of the background channel (fiber 24) from that of CXS channel (fiber 23) at $t=0.6$ s, where the poloidal rotation velocity is small. The fitting curve of the hot component is given by multi-Gaussian fitting with a common Doppler width using the intensity ratio of each component of the fine structure of the beam (80 keV) C VI line. As shown in Fig. 6(b), the cold component is well fitted by the fine structure of the thermal (0.2 keV) O VI line, while there is a clear discrepancy in the fitting curve using a fine structure of the thermal (0.2 keV) C VI line. This is because there is a difference of 0.012 nm in the mean wavelength between the thermal C VI line and the thermal O VI line. The mean wavelength is determined by the intensity ratio as well as by the wavelength of each component of the fine structure. Therefore the mean wavelength depends on the electron density of the plasma, because the population of each l sublevel is redistributed by the l-mixing and cascade effect. However, the dependence of the mean wavelength on the plasma density is weak and the change in the mean wavelength due to the l-mixing is much smaller than the differences in mean wavelength between the thermal C VI line and the thermal O VI line as shown in Fig. 7. It should be noted that the mean wavelength of the thermal C VI line is longer than the mean wavelength of the beam C VI line (529.055 nm) by 3 pm, while that of the O VI line is shorter than that of the beam C VI line by 9 pm. The measured difference in the mean wavelength between the CXS channel and BKG channel is -8 pm and is consistent with the differences of the mean wavelength between the beam C VI line and the thermal O VI line, which implies a large contribution by the O VI line to the cold component. The mean wavelength of BKG channels depends on the fraction of O VI and C VI contributions to the cold component. It is 4 pm for the plasma where the O VI contribution is reduced by titanium (Ti) gettering.

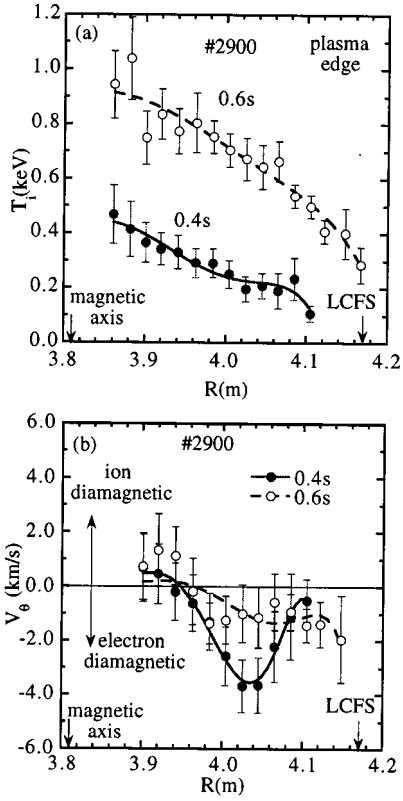

FIG. 8. Radial profiles of (a) ion temperature and (b) poloidal rotation velocity measured with charge exchange spectroscopy in a LHD. The positive poloidal rotation velocity stands for a plasma rotation in the ion diamagnetic direction, while negative values stand for a rotation in the electron diamagnetic direction.

V. MEASUREMENTS OF ION TEMPERATURE AND POLOIDAL ROTATION PROFILES

Figure 8 shows the radial profiles of ion temperature and poloidal rotation velocity measured with C VI for LHD plasmas with a magnetic field of 1.5 T, central electron density of 1.0×10^{19} m^{-3}, and electron temperature of 1.1 keV. The central ion temperature is 0.9 keV which is slightly lower than the central electron temperature. The magnetic axis is located at $R=3.84$ m due to a finite β shift ($R=3.75$ m for a vacuum magnetic field). The plasma edge is at $R=4.18$ m. Because the cross section between the NBI and the line of sight of CXS is restricted only at $R=3.8$–4.2 m (the center of the NBI does not match the center of the plasma and it is $R=4.0$ m at the poloidal cross section in the port for charge exchange spectroscopy), there is no measurement of the ion temperature inner half of the plasma ($R<3.8$ m). The radial profiles of poloidal rotation velocity are calculated from the difference of the Doppler shift from the average of the nearby Doppler shift. At $t=0.4$ s, the radial profile of the poloidal rotation velocity has a peak of -4 km/s in the elec-

tron diamagnetic direction (negative electric field) at $R = 4.03$ m, and the poloidal rotation is small at $t = 0.6$ s. As seen in Fig. 7(a), the ion temperature is low at $t = 0.4$ s and ion collision frequency is higher and plasma rotates more in the electron diamagnetic direction at $t = 0.4$ s. As the plasma temperature increases over time, ion collision frequency and poloidal rotation in electron diamagnetic direction decrease, which is qualitatively consistent with that predicted by neoclassical theory.

Absolute measurements of poloidal rotation velocity with accuracy up to 1 km/s were done using charge exchange spectroscopy with four sets of optical fiber arrays viewing downward and viewing upward at the poloidal cross sections with and without NBI in a LHD. The measured poloidal rotation velocity is 1–3 km/s in the electron diamagnetic direction at half of the plasma minor radius.

ACKNOWLEDGMENTS

The authors would like to thank Dr. H. Summers (JET) for providing them with the results of ADAS. The authors also thank the experiment groups and technical support staff of LHD.

[1] R. C. Isler, L. E. Murray, S. Kasai, J. L. Dunlap, S. C. Bates, P. H. Edmonds, E. A. Lazarus, C. H. Ma, and M. Murakami, Phys. Rev. A **24**, 2701 (1981).
[2] R. J. Fonck, M. Finkenthal, R. J. Goldston, D. L. Herndon, R. A. Hulse, R. Kaita, and D. D. Meyerhofer, Phys. Rev. Lett. **49**, 737 (1982).
[3] R. J. Groebner, N. H. Brooks, K. H. Burrell, and L. Pottler, Appl. Phys. Lett. **43**, 920 (1983).
[4] R. J. Fonck, D. S. Darrow, and K. P. Jaehnig, Phys. Rev. A **29**, 3288 (1984).
[5] R. P. Seraydarian, K. H. Burrell, N. H. Brooks, R. J. Groebner, and C. Kahn, Rev. Sci. Instrum. **57**, 155 (1986).
[6] K. Ida and S. Hidekuma, Rev. Sci. Instrum. **60**, 867 (1989).
[7] H. Weisen, M. von Hellermann, A. Boileau, L. D. Horton, W. Mandl, and H. P. Summers, Nucl. Fusion **29**, 2187 (1989).
[8] A. Kallenbach, H.-M. Mayer, G. Fussmann, R. Buchse, O. Gruber, O. Kluber, V. Mertens, O. Vollmer, and H. Zohm, Nucl. Fusion **30**, 645 (1990).
[9] R. C. Isler, Plasma Phys. Controlled Fusion **36**, 171 (1994).
[10] R. J. Groebner, K. H. Burrell, and R. P. Seraydarian, Phys. Rev. Lett. **64**, 3015 (1990).
[11] K. Ida, S. Hidekuma, Y. Miura, T. Fujita, M. Mori, K. Hoshino, N. Suzuki, T. Yamauchi, and JFT-2M group, Phys. Rev. Lett. **65**, 1364 (1990).
[12] J. Kim, K. H. Burrell, P. Gohil, R. J. Groebner, Y. B. Kim, H. E. St. John, R. P. Seraydarian, and M. R. Wade, Phys. Rev. Lett. **72**, 2199 (1994).
[13] K. Ida, H. Yamada, H. Iguchi, K. Itoh, and CHS group, Phys. Rev. Lett. **67**, 58 (1991).
[14] H. Wobig, H. Maassberg, H. Renner, W. VII Team, ECRH group, and NI group, *Proceedings of 11th International Conference, Kyoto, 1986* (IAEA, Vienna, 1987), Vol. II, p. 369.
[15] K. Ida, H. Yamada, H. Iguchi, S. Hidekuma, H. Sanuki, K. Yamazaki, and CHS group, Phys. Fluids B **3**, 515 (1991); **4**, 1360 (1992).
[16] K. Ida *et al.*, Phys. Rev. Lett. **76**, 1268 (1996).